

Depth Completion Using a View-constrained Deep Prior

Pallabi Ghosh
University of Maryland
pallabig@cs.umd.edu

Vibhav Vineet
Microsoft Research
Vibhav.Vineet@microsoft.com

Larry S. Davis
University of Maryland
lsd@cs.umd.edu

Abhinav Shrivastava
University of Maryland
abhinav@cs.umd.edu

Sudipta N. Sinha
Microsoft Research
Sudipta.Sinha@microsoft.com

Neel Joshi
Microsoft Research
neel@microsoft.com

Abstract

Recent work has shown that the structure of convolutional neural networks (CNNs) induces a strong prior that favors natural images. This prior, known as a deep image prior (DIP), is an effective regularizer in inverse problems such as image denoising and inpainting. We extend the concept of the DIP to depth images. Given color images and noisy and incomplete target depth maps, we optimize a randomly-initialized CNN model to reconstruct a depth map restored by virtue of using the CNN network structure as a prior combined with a view-constrained photo-consistency loss. This loss is computed using images from a geometrically calibrated camera from nearby viewpoints. We apply this deep depth prior for inpainting and refining incomplete and noisy depth maps within both binocular and multi-view stereo pipelines. Our quantitative and qualitative evaluation shows that our refined depth maps are more accurate and complete, and after fusion, produces dense 3D models of higher quality.

1. Introduction

There are numerous approaches for estimating scene depth, such as using binocular [42] or multi-view [13, 20, 44] stereo, or directly measuring depth with depth cameras, *e.g.* LIDAR, *etc.* These approaches suffer from artifacts, such as noise, inaccuracy, and incompleteness, due to various limitations. As depth estimation is an ill-posed problem, extensive research has been conducted to solve the problem using approximate inference and optimization techniques that employ appropriate priors and regularization [8, 51, 52, 60].

Supervised learning methods based on convolutional neural networks (CNNs) have shown promise in improving depth estimations, both in the binocular [28, 35, 64] and multi-view [26, 27, 62] stereo settings. However, these supervised methods rely on vast amounts of ground truth data

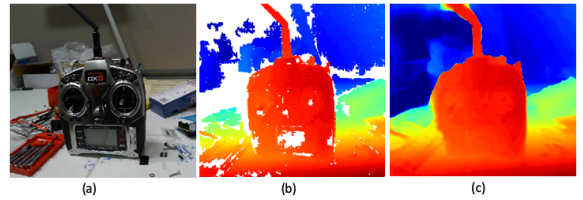


Figure 1. (a) Input image from one viewpoint (b) Target depth map computed with SGM using neighboring images[24] (c) The refined depth map generated using our deep depth prior (DDP). Depth map (c) has the holes from (b) (shown in white) filled.

to achieve proper generalization. While unsupervised learning approaches have been explored [38, 54, 66], their success appears modest compared to supervised methods.

In this work, we propose a new approach for improving depth measurements that is inspired by the recent work by Ulyanov *et al.* [56]. They demonstrated that the underlying structure of an encoder-decoder CNN induces a prior that favors natural images, a property they refer to as a “deep image prior” (DIP).

Ulyanov *et al.* show that the parameters of a randomly initialized encoder-decoder CNN can be optimized to map a high-dimensional noise vector to a single image. When the image is corrupted and the optimization is stopped at an appropriate point before overfitting sets in, the network outputs a remarkably noise-free image. The DIP has since been used as a regularizer in a number of low-level vision tasks such as image denoising and inpainting [16, 56, 59].

In this work, we propose using DIP-based regularization for refining and inpainting noisy and incomplete depth maps. Our approach can be used to refine depth maps obtained from a wide variety of sources.

Using a network similar to Ulyanov *et al.*, our approach generates a depth map by combining a depth reconstruction loss with a view-constrained photoconsistency loss. The latter loss term is computed by warping a color image into

neighboring views using the generated depth map and then measuring the photometric discrepancy between the warped image and the original image.

In this sense, our technique resembles direct methods proposed decades ago for image registration problems, which all employ some form of initialization and iterative optimization. However, instead of using handcrafted regularizers in the optimization objective, we use the deep image prior as the regularizer. While the role of regularization in end-to-end trainable CNN architectures is gaining interest [31, 61], our method is quite different, because there is no training and the network parameters are optimized from scratch on each set of test images. Figure 1 shows the inpainting results of applying our technique (DDP) on an input depth map with holes.

To the best of our knowledge, this is the first work to investigate deep image priors for completing depth images. We evaluate our approach using results from modern stereo pipelines and depth cameras and show that the refined depth maps are more accurate and complete, leading to more complete 3D models.

2. Related Work

Stereo matching. Dense stereo matching is an extensively studied topic and there has been tremendous algorithmic progress both in the binocular setting [24, 31, 35, 64, 66] as well as in the multi-view setting [14, 21, 26, 44, 62], in conjunction with advances in benchmarking [1, 18, 29, 40, 45]. Traditionally, the best performing stereo methods were based on approximate MRF inference on pixel grids [8, 51, 60], where including suitable smoothness priors was considered quite crucial. However, such methods were usually computationally expensive. Hirschmuller [24] proposed Semi-Global Matching (SGM), a method that provides a trade-off between accuracy and efficiency by approximating a 2D MRF optimization problem with several 1D optimization problems. SGM has many recent extensions [5, 17, 43, 46, 48] and also works for multiple images [21]. Region growing methods have also shown promise and implicitly incorporate smoothness priors [7, 22, 33, 44].

Deep Stereo. In recent years, deep models for stereo have been proposed to compute better matching costs [10, 34, 64] or to directly regress disparity or depth [9, 28, 35, 66] and also for the multi-view setting [26, 27, 62]. Earlier on, end-to-end trainable CNN models did not employ any form of explicit regularization, but recently hybrid CNN-CRF methods have advocated using appropriate regularization based on conditional random fields (CRFs) [31, 61]. In contrast with these works, as we do not perform learning by fitting to training data, our approach is more generalizable as it does not fall prey to the tendency of deep approaches to overfit to their training data.

Depth Map Refinement/Completion. The fast bilateral solver [6] is an optimization technique for refining disparity or depth maps. However, the objective is fully hand-crafted. Knoblereiter and Pock recently proposed a refinement scheme where the regularizer in the optimization objective is trained using ground truth disparity maps [30]. Their model learns to jointly reason about image color, stereo matching confidence and disparity. Voynov *et al.* [57] use a deep prior for depth super-resolution, but they do not have a multiview constraint, as we do, nor do they investigate refinement and hole-filling. Other recent disparity or depth map refinement techniques utilize trained CNN models [37]. Similarly depth map completion by Zhang and Funkhouser [65] use a learning based technique. They do single RGBD image depth completion whereas we use a multi-view photo-consistency loss for training our network. Also we show in our results that one main difference between their work and ours is that our result is not dependent on training data distributions. Depthcomp [3] also does depth completion and they use the semantic segmentation maps as prior knowledge.

Deep prior for color images. Beyond the previously discussed work of Ulyanov *et al.* [56], deep image priors have been extended for a number diverse applications – neural inverse rendering [50], mesh reconstruction from 3D points [59], and layer-based image decomposition [16]. Recently, Cheng *et al.* [11] pointed out important connections between DIP and Gaussian processes. Our approach is in a similar vein as these approaches, where we modify the DIP for depth maps by combining the usual reconstruction loss with a second term, the photoconsistency loss which ensures that when the reference image is warped into a neighboring view using our depth map, the discrepancy between the warped image and the original image is minimized.

3. Method

Given a RGBD image with I^{in} as RGB component and D^{in} as noisy depth component, our goal is to generate denoised and inpainted depth image D^* . We leverage recently proposed Deep Image Prior (DIP) [56] to solve this problem. We first briefly describe the DIP approach.

3.1. Deep Image Prior

The DIP method proposed a deep network based technique for solving low level vision problems such as image denoising, restoration, inpainting, *etc.* At the core of their method lies the idea that deep networks can serve as a prior for such inverse problems. If x is the input image, n is the input noise and x_o is the denoised output of the network f_θ , then the optimization problem of the DIP method takes the following form:

$$\theta^* = \arg \min_{\theta} L(f_\theta(n); x), \quad x_o^* = f_{\theta^*}(n). \quad (1)$$

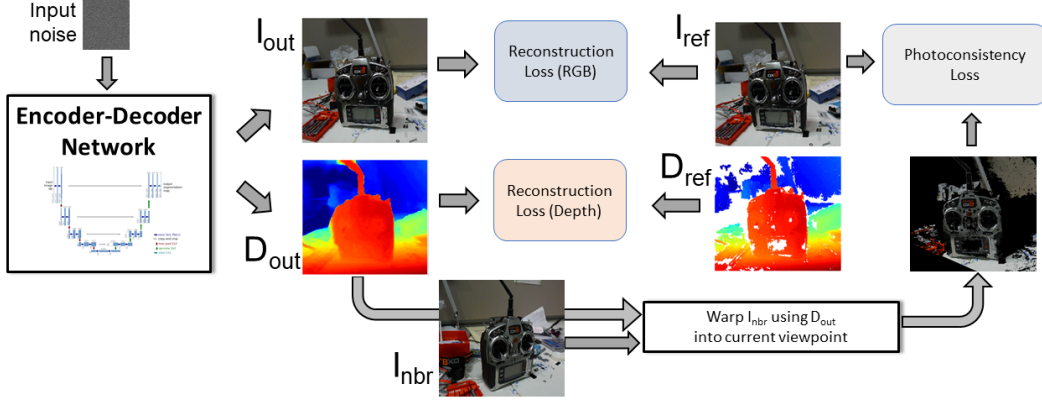


Figure 2. Overview of the Deep Depth Prior (DDP): The DDP network is trained using a combination of L1 and SSIM reconstruction loss with respect to a target RGB-D image and a photoconsistency loss with respect to neighboring calibrated images. This network is used to refine a set of noisy depth maps and the refined depth maps are subsequently fused to obtain the final 3D point cloud model. I^{out} and D^{out} are the RGB and depth output of our network. I^{nbr} is the RGB at a neighboring viewpoint. I^{ref} and D^{ref} are the input RGB and depth at the current (reference) viewpoint.

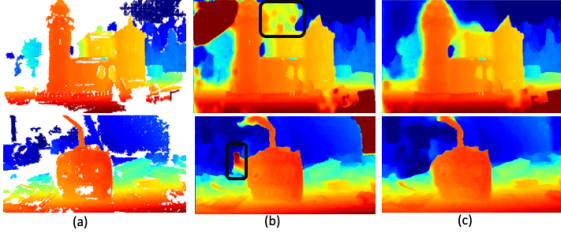


Figure 3. (a) Input depth map with holes (b) DDP on just depth maps and (c) DDP on RGBD images. In the black box regions in (b), DDP is filling up the holes in the sky or background based on the depth from the house or radio because it has no edge information. RGBD input provides this edge information in (c).

The task of finding the optimal neural network parameters θ^* and the optimal denoised image x_o^* is solved using the standard backpropagation approach.

A simple approach to address depth denoising and inpainting would be to use a DIP like encoder-decoder architecture to improve the depth images. Here depth images would replace RGB as inputs in the original DIP framework. However this fails to fill the holes with correct depth values. Some of the results are shown in Figure 3. More quantitative results are provided in Table 2. We hypothesize three reasons for this failure. First, holes near object boundary can cause incorrect depth filling. Second, depth images have more diverse values than RGB images that leads to large quantization errors. Finally absolute error for far objects may dominate the DIP optimization over important nearby objects.

3.2. Deep Depth Prior

In this work, we propose the Deep Depth Prior (DDP) and introduce three losses to solve the issues discussed

above. Our approach is built on top of the inpainting task in Ulyanov *et al.* [56] where we create a mask for the holes in the depth map and calculate the loss over the non-masked regions. Figure 2 gives an overview of our system.

To solve the issue of absolute error for far objects dominating the DIP optimizer, inverted depth or disparity images are used. We also add a constant value to depth image that reduces the ratio between the maximum and minimum depth values. Further, masking of all far away objects beyond a certain depth is performed by clipping to a predefined maximum depth value. We also clip depth to a minimum value so that the maximum disparity value does not go to infinity. We provide these values and values of the loss hyper-parameters in the supplementary.

Let D^{out} be the desired depth output from our network and let f_θ denote the generator network. Input to the network is noise n^{in} and the input depth map is inverted to get Z^{in} as the noisy disparity map. Let us represent the output from the network as Z^{out} where $Z^{out} = f_\theta(n^{in}; Z^{in})$. On convergence, optimal D^* is obtained by inverting Z^* .

We use three different losses to optimize our network. The total loss is defined as follows.

$$L^{total} = \gamma_1 L^{disp} + \gamma_2 L^{RGB} + (1 - \gamma_1 - \gamma_2) L^{warp}. \quad (2)$$

Disparity-based loss (L^{disp}). The simplest technique to obtain Z^* is to optimize only on disparity. The disparity based loss L^{disp} is a weighted combination of Mean Absolute Error (MAE) or L^1 loss and Structural Similarity metric (SSIM) or L^{SSIM} loss [58], and takes the following form:

$$L^{disp} = \lambda_z L^1(Z^{in}, Z^{out}) + (1 - \lambda_z) L^{SSIM}(Z^{in}, Z^{out}). \quad (3)$$

We use L^1 loss instead of Mean Squared Error (L^2) loss to remove the effect of very high valued noise having a

major effect on the optimization. It takes the form as $L^1(Z^{\text{in}}, Z^{\text{out}}) = |Z^{\text{in}} - Z^{\text{out}}|$. The structural similarity L^{SSIM} loss measures similarity between the input Z^{in} and reconstructed disparity map Z^{out} . Here similarity is defined at the block level where each block size is 11×11 . It provides consistency at the region level. The loss (L^{SSIM}) takes the following form $L^{\text{SSIM}} = 1 - \text{SSIM}(Z^{\text{in}}, Z^{\text{out}})$. Details about SSIM are provided in the supplementary.

RGB-based loss (L^{RGB}). We observed that under certain situations the disparity based loss leads to blurred edges in the final generated depth map. This happens when there is a hole in the depth map near an object boundary. The generator network produces a depth map that fuses the depths of different objects appearing around the hole.

For example, consider regions belonging to sky in the top row of Figure 3. Due to the homogeneous nature of the sky pixels, standard disparity/depth estimation methods fail to produce any valid values for such regions. However, pixels corresponding to house region have depth values. When the image is passed to a DIP generator, the edge between the house and the sky gets blurred because the network is trying to fill up the space without any additional knowledge, e.g., boundary information. It just bases its decision on depth of neighboring space to fill up the incomplete regions as seen in the top row of Figure 3(b) in the black box region.

To solve this problem, we also pass the color RGB image along with the disparity image. The encoder-decoder based DDP architecture is now trained on the 4 channel RGBD image. The network weights are updated not only on the masked disparity map but also on the full RGB image. This helps the network to leverage edge and texture information for the object boundary in the RGB image to fill the holes in the disparity (and so in depth) image. This important edge information provided to the network helps to generate crisp depth images as seen in the Figure 3(c).

Let I^{out} be the output corresponding to input data I^{in} using the noise n^{in} and generator model f_{θ} . It takes the form as $I^{\text{out}} = f_{\theta}(n^{\text{in}}; I^{\text{in}})$. The Loss L^{RGB} is also a weighted combination of L^1 and SSIM losses, and is defined as:

$$L^{\text{RGB}} = \lambda_I L^1(I^{\text{in}}, I^{\text{out}}) + (1 - \lambda_I) L^{\text{SSIM}}(I^{\text{in}}, I^{\text{out}}). \quad (4)$$

The RGB based loss helps to resolve the issue of blurring observed around edges near object boundaries. However, putting equal weights to disparity (L^{disp}) and RGB (L^{RGB}) components of the total loss leads to artifacts appearing in the disparity image and so in depth output images as well. In particular, these artifacts are due to textures and edges from an object’s appearance that are unrelated to the depth boundaries. For example in Figure 4 the wall of the house is one surface and should have smooth depth maps. However, the DDP network trained on RGBD data generates vertical textures in the depth images that appear due to the vertical wooden planks in the RGB image.

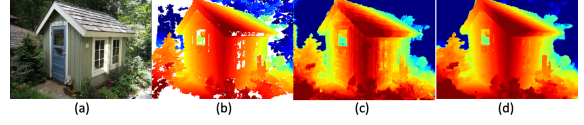


Figure 4. (a) RGB image (b) Input disparity map (c) Disparity output from DDP trained with equal weight for RGB and depth loss. The RGB artifacts are evident in (c) through the vertical and horizontal lines representing the wooden planks in the wall (d) Disparity output from the DDP trained with lower weight for the RGB loss compared to depth loss. The artifacts disappear in (d).

Warping-based loss (L^{warp}). Lastly, we include a warping loss. Before defining the warping loss, let us first define the warping function $T_{\text{nbr}}^{\text{ref}}$. Given the camera poses C_{ref} and C_{nbr} of the reference and neighboring view, the function $T_{\text{nbr}}^{\text{ref}}$ warps neighboring view to reference view.

We are trying to generate denoised output Z^{out} for the reference view. We first find top N neighboring views of the reference view using the method used in MVSNet [62] for the multi-view pipeline. Let nbr denote one of these N views and let $W_{\text{nbr}}^{\text{ref}}$ be the warped image from neighboring view to reference view. Let $D_{\text{ref}}^{\text{out}}$ be the predicted depth (inverted $Z_{\text{ref}}^{\text{out}}$) for the reference view and $I_{\text{nbr}}^{\text{in}}$ is the input RGB for the neighboring view, then the warped image is $W_{\text{nbr}}^{\text{ref}} = T_{\text{nbr}}^{\text{ref}}(D_{\text{ref}}^{\text{out}}, I_{\text{nbr}}^{\text{in}}; C_{\text{nbr}}, C_{\text{ref}})$. Further, we use bilinear interpolation while warping.

Now given $I_{\text{ref}}^{\text{in}}$, the input RGB for the reference view, we can compute warping loss as:

$$L_{\text{nbr-ref}}^{\text{warp}} = \lambda_w L^{\text{SSIM}}(I_{\text{ref}}^{\text{in}}, W_{\text{nbr}}^{\text{ref}}) + (1 - \lambda_w) L^1(I_{\text{ref}}^{\text{in}}, W_{\text{nbr}}^{\text{ref}}). \quad (5)$$

When there are multiple neighboring views, the loss is averaged over them as $L_{\text{ref}}^{\text{warp}} = \frac{1}{N} \sum_{\text{nbr}=1}^N L_{\text{nbr-ref}}^{\text{warp}}$.

The warping loss helps to improve the accuracy of the disparity (and depth) values and the importance of each loss term is explored further in section 4.

Optimization. All three losses that we use are differentiable with respect to the network parameters and so the network is optimized using standard backpropagation.

4. Experiments

We demonstrate the effectiveness of our proposed approach on two different tasks - 1) depth completion and 2) depth refinement. We also show the generalization ability of our technique on new datasets with unseen statistical distributions. We applied the deep depth prior on multi-view and stereo pipelines and evaluate results on five different datasets: 1) Tanks and Temples (TnT) [29], 2) KITTI stereo benchmark [18, 36], 3) Our own collected videos, 4) NYU depth V2 [47] and 5) Middlebury Dataset [25, 41]. In all our experiments, the base network is primarily an encoder-decoder (UNet) architecture [39]. The UNet encoder consists of 5 convolution blocks each consisting of 32, 64, 128,

Table 1. We compare the f-score of DDP on datasets of different sizes. As the number of images become smaller, the holes increase and the most relative performance gain is at 22 images. We also compare to [65] applied to an data that is out of distribution and show we do better. Higher is better.

Dataset	SGM	SGM+ [65]	SGM+ DDP (Ours)
Ignatius(87 images)	45.3	45.2	45.6
Ignatius(44 images)	44.0	44.0	44.2
Ignatius(22 images)	30.7	30.7	31.1

Table 2. We show results of comparing the DDP output using disparity, RGBD, and warping loss and using UNet/SkipNet. P: precision, R: recall, F: f-Score. Higher is better.

Network + Loss	P	R	F
UNet + D	34.3	37.2	35.7
UNet + RGBD	39.2	49.0	43.6
UNet + RGBD + warp	40.0	50.6	44.7
SkipNet + RGBD + warp	40.2	50.3	44.7

256, and 512 channels. Each convolution operation uses 3x3 kernels. We also conducted experiments using skip networks [56]. The input noise to the network is of size $m \times n \times 16$, where m and n are the dimensions of the input depth images. Training is performed using the Adam optimizer. Details about learning rate and scheduler are provided in the supplementary.

4.1. Tanks and Temples

We evaluate the effectiveness of the presented approach on the multi-view reconstruction task through qualitative and quantitative improvement on seven sequences from the Tanks and Temples dataset (TnT dataset) [29]. These sequences include Ignatius, Caterpillar, Truck, Meetingroom, Barn, Courthouse, and Church. To reconstruct the final 3D point cloud the depth images are fused using the approach proposed by Galliani *et al.* [15] (Fusibile). Fusibile has hyperparameters that determine the precision and recall values for the resultant point cloud. These parameters include the disparity threshold and the number of consistent views. More details about Fusibile and loss hyper-parameters are provided in the supplementary material.

Quantitative results. Our primary comparison is with the popular semi-global matching (SGM) method [24] for depth image estimation. SGM is an optimization based method that does not need any training data. We also compare with a state-of-the-art learning based method: MVS-Net [62]. Further, it should be noted that our approach is agnostic to the depth estimation method, i.e., it can be used to improve depth maps from any source.

We compare our reconstructed point clouds to the ground truth point clouds for all 7 sequences in the TnT

Table 3. Quantitative results comparing 7 sequences for SGM based depths and applying DDP on SGM depths. We combine DDP with SGM by replacing the depth values in the holes of SGM depth with DDP depth. Here the datasets are I: Ignatius, B: Barn, T: Truck, C1: Caterpillar, MR: Meetingroom, CH: Courthouse, and C2: Church. N: number of images in a sequence, C: number of consistent views while constructing point cloud, D: disparity threshold, P: precision, R: recall, F: f-score. Higher is better.

Data	N	C	D	SGM			SGM+DDP(Ours)		
				P	R	F	P	R	F
I	87	5	1.0	41.7	49.5	45.3	41.2	51.1	45.6
I	22	2	2.0	32.7	29.0	30.7	32.2	30.1	31.1
B	180	2	0.5	23.3	27.8	25.4	22.8	29.3	25.6
B	45	1	4.0	19.1	21.4	20.2	18.1	22.8	20.2
T	99	4	1.0	35.8	38.8	37.2	34.5	41.4	37.6
T	25	1	2.0	29.4	33.8	31.5	27.7	36.7	31.6
C1	156	4	1.0	24.9	41.5	31.1	24.0	42.9	30.8
C1	39	1	2.0	17.3	36.5	23.5	16.2	37.9	22.7
MR	152	4	1.0	27.5	13.4	18.1	25.2	15.2	19.0
MR	38	1	4.0	17.8	9.0	12.0	15.7	10.7	12.7
CH	110	2	1.0	1.8	0.8	1.1	3.2	1.2	1.7
C2	86	4	1	8.9	8.5	8.7	8.9	8.6	8.8

dataset [29], using the benchmarking code included with the dataset, which returns the precision ($P = \frac{TP}{TP+FP}$), recall ($R = \frac{TP}{TP+FN}$) and f-score ($F = 2 \cdot \frac{PR}{P+R}$) values for each scene given the reconstructed point cloud model and a file containing estimated camera poses used for that reconstruction. Here, TP , FP , and FN are true positives, false positives, and false negatives respectively. For each of the sequences we report values at the same points of the precision-recall curve as specified by the TnT dataset.

Ablation studies. We conduct a series of experiments on the Ignatius dataset to study impact of each parameter and component of the proposed method. We first study the effect of number of depth images on the final reconstruction. For this purpose, we skip a constant number of images in the dataset. For example, a skip size of 2 means that only every second image is used for reconstruction giving us 87 images in total for Ignatius. Such reduction in the data size increases the number of holes on the SGM-based reconstruction method. The same reduced dataset is used for the baseline and our approach. One of the goals of this work is for our accurate hole-filling to allow for fewer images to be captured and used for reconstruction. We also conducted experiments with skip values of 4 and 8 giving 44 and 22 images. Table 1 provides details about the impact of this skip size on relative improvement. For SGM+DDP, we keep SGM values where there are no holes, and replace the holes with DDP output values in those regions. It can be observed that at skip sizes of 2, 4 and 8, we see an improvement of 0.3, 0.2 and 0.4 percentage point of relative improvement in f-scores over the baseline respectively. It suggests that

Table 4. We compare the reconstruction performance using depth maps generated by MVSNet and by applying DDP on MVSNet. I: Ignatius, P: precision, R: recall, F: f-score. Higher is better.

Dataset	MVSNet			MVSNet + DDIP		
	P	R	F	P	R	F
I (126 images)	45.9	52.2	48.8	45.2	54.9	49.6
I (32 images)	40.3	46.8	43.3	38.9	50.0	43.8

at higher skip sizes, our approach provides necessary prior information to fill holes. Please note that we have not included experiments with skip size of one. Running Fusibile on all of the Ignatius images produces dense reconstruction without holes. Running DDP on this dense reconstruction has no effect, and so we have not included results with skip size of one in the table. Table 1 also contains results in comparison to Zhang and Funkhouser [65] which we will discuss later.

Next we show the advantage of using the RGBD and warping losses over disparity loss only. Running the optimization for too many epochs on the depth only DDP can return the holes in the result, thus we run the depth only based networks for 6000 epochs instead of 16000. The results are in Table 2, showing a 7.9% improvement in f-measure by using RGBD. Table 2 also shows the benefit of photo-consistency based warping loss. We observe a relative improvement of 1.1% in f-measure after incorporation of the warping loss. Finally, we also conducted experiments with Skip-Net [56] to show the impact of using a network different from UNet. Table 2 shows they give comparable results, and we chose to use UNet for our other experiments since it is a more commonly used network.

Comparison to prior work. Quantitative comparison with the SGM baseline on the 7 TnT dataset is shown in the Table 3. The SGM+DDP (Ours) column shows the results of using DDP to improve depth maps from SGM. We combine DDP depth maps with SGM depth maps, keeping the SGM values everywhere where there are no holes and replace the holes with DDP depth values. The table includes the precision, recall and f-scores on each dataset with subsampled number of images using the technique described in the Ablation Studies sub-section. We observe improvement in both recall and f-score values of the presented approach over the SGM-method. It suggests the method helps in hole filling. The f-score improves in 6 of the 7 sequences. Overall SGM+DDP(Ours) helps to improve recall by 1.5 percentage points and f-score by 0.2 percentage points. In particular, we see a significant improvement of 1.8 in recall and 0.8 in f-score on the MeetingRoom sequence.

We also test using the learning-based MVSNet method as an input to our method. While the results from MVSNet do not contain any holes, as they predict a value at every pixel, just as we do, they do have areas where the predic-

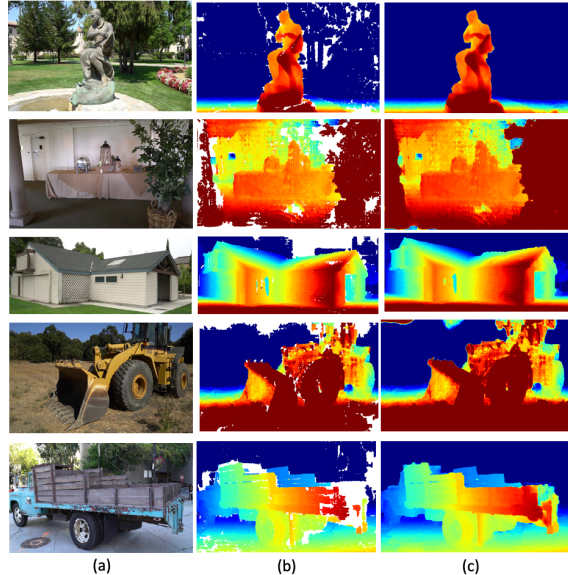


Figure 5. (a) Input RGB and (b) Input depth images and (c) Predicted depth at 16000 epochs for Ignatius, Meeting Room, Barn, Caterpillar and Truck. (Best viewed in digital. Please zoom in.)

tions have low confidence. We use their output probability map which shows confidence of depth prediction and remove depths at places with confidence below a certain threshold (0.1) to see if we can fill those areas more accurately than MVSNet did. We then fill up these holes using DDP and compare the results with the original. These results for Ignatius are in Table 4. We see 0.7% improvement in F-score and 3.0% in recall.

Finally we compare to Zhang and Funkhouser [65] in Table 1. We use the trained networks provided by Zhang and Funkhouser using SUNCG-RGBD [49] and ScanNet [12] datasets for inpainting on Ignatius dataset. As we can see here this method does not work well because it is a learning based system. Ignatius is an out-of-distribution test data and the model would require finetuning. This emphasizes the usefulness of our network being optimized at test time and it being independent of training data statistics.

Qualitative results. Next we provide visual results on the TnT dataset to highlight the impact of our approach in achieving high quality reconstruction. In Figure 5, we show output disparity images at 16000 (column c) epochs of our proposed approach on 5 TnT sequences. Note that the holes in the input disparity images (marked as white in column b) are filled in the output images (c).

4.2. KITTI

Next we show the performance of the proposed approach on the KITTI stereo benchmark (2015) [36] for 3 different input disparity maps in Table 5. The evaluation metrics used is D1 that measures the error percentage when the predicted value differs from the groundtruth value by 3 pixels or 5%

Table 5. Results on KITTI Dataset using D1 error. Lower is better.

Method	D1-bg	D1-fg	D1-all
ELAS (params1)	7.5	21.1	9.8
ELAS+DDP (params1)	7.5	21.1	9.7
ELAS (params2)	20.6	28.7	22.0
ELAS+DDP (params2)	12.3	20.2	13.6
HD3	1.78	3.64	2.09
HD3+DDP	1.75	3.55	2.05
HD3 trained on [35]	78.74	79.16	78.81

or more. This error is separately measured for background, foreground and all regions together. 3 approaches to generate input depths for DDP are as follows:

1. We use first set of parameters for ELAS [19] to generate disparity maps without holes and DDP for refinement and completion. We observe a small performance improvement ($\sim 0.1\%$ reduction in D1-all error).
2. We use a second set of parameters for ELAS to generate depth images with holes. In this case, DDP applied over ELAS depth helps to inpaint and complete the ELAS depth with a 8.4% reduction in D1-all error.
3. We take the output of a state of the art deep learning based stereo estimation technique, HD3 [63], as the input to our method. We removed depth values in the depth maps where the reported confidence equals 0.0, and then ran our approach to fill those areas with more accurate depth values. Using our approach we get an improvement of 0.09% on the foreground objects and 0.04% overall. HD3 trained and tested on the KITTI dataset outputs complete and accurate depth maps and so we observe small improvement by applying DDP. For sample point of an out-of-distribution model, we used HD3 model trained on the FlyingThings3D dataset [35]. ELAS (which does not use deep learning) does 69 percentage point better. It highlights that our approach with traditional stereo methods can work well under different environment conditions.

4.3. Our dataset

We used an off-the-shelf consumer camera to capture 5 scenes, both indoor and outdoor. The datasets are monocular image sequences and are named Guitar, Shed, Stones, Red Couch, and Van.

To better understand the quality of the depth images generated by the proposed method, we warp RGB images using the original and the proposed DDP based depth images for Shed and Stones from our video sequences and Truck from TnT dataset. The warped RGB images are shown in the Figure 6. Holes can be observed in the RGB images warped using original depth maps for example along the

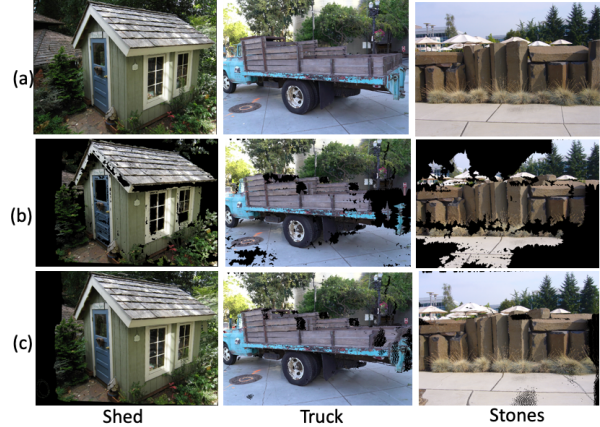


Figure 6. (a) Input image from the reference view point (b) Novel view synthesized from neighboring to reference viewpoint using the SGM depth (c) Novel view synthesis from a neighboring to reference viewpoint using DDP depth. The holes that appear in (b) gets filled in (c). (Best viewed in digital. Please zoom in.)

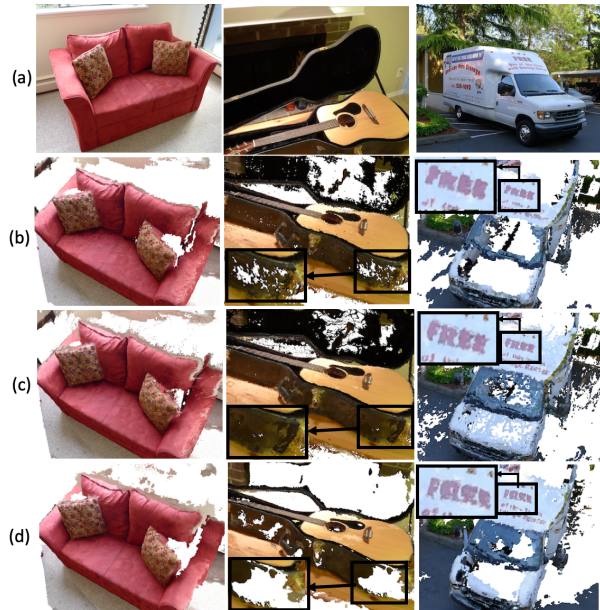


Figure 7. (a) Input RGB image and reconstructed point-cloud from (b) SGM (c) DDP (Ours) and (d) MVSNet depth images for Red-Couch, Guitar and Van. Our reconstructions are better and more complete. (Best viewed in digital. Please zoom in.)

roof of the shed, some parts of the truck and along the base of the Stone Wall. However, RGB images warped using our depth images removes large portions of these holes and are far smoother.

We show reconstructed point clouds on RedCouch, Guitar and Van in Figure 7. The first row is one of the input RGB images used for the reconstruction, second row is the reconstruction from the original SGM output, the third one is from SGM + DDP, and the fourth row is the reconstructed

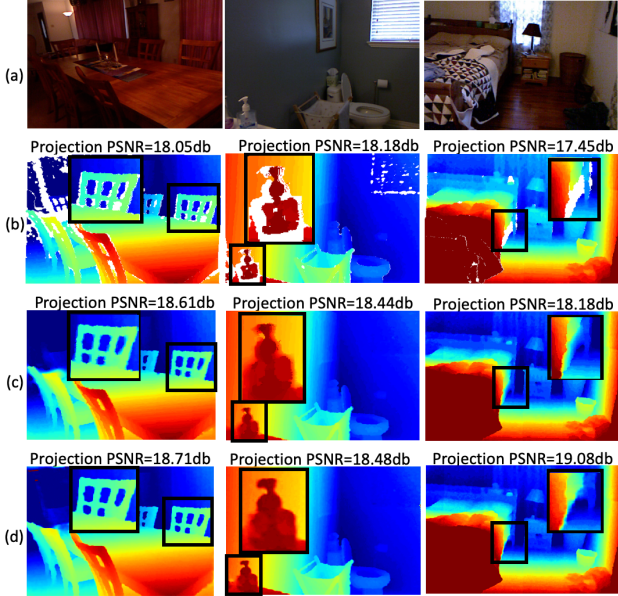


Figure 8. (a) Input RGB (b) Input depth (c) Depth completed using a cross-bilateral filter and (d) Depth completed using DDP. (Best viewed in digital. Please zoom in.)

result from MVSNet. The number of views used for these reconstructions are small (~ 10). We chose these datasets to show specific ways in which our reconstructions improve on the original SGM and even MVSNet outputs. As we can see from our results, there are a lot less holes in the reconstructions computed from our depth maps compared to original SGM and MVSNet. For example from the top view of the RedCouch in the first column, we can see the relatively obscure region behind the pillow. The DDP successfully fills up a big portion of this hole. Next the reflective surfaces of the guitar in the second column and the van in the third column also get completely or at least partially filled depending on how big the original hole was. For example note how the text “FREE” on the van is more readable in the DDP result.

4.4. NYU v2

We demonstrate performance of our approach on hole-filling Kinect depth data. For this, we use data from the popular NYU v2 dataset [47]. Qualitative experiments on the NYU v2 depth images are shown in Figure 8. We cannot directly use the test data from NYU, since we need at least two views as input. So we downloaded 3 video scenes, and used a structure-from-motion (SfM) pipeline [55] to get the extrinsic camera pose information. Using this, we apply DDP to remove holes in the Kinect depth maps given by the dataset. We directly refined the Kinect depth images, and as the originals are incomplete, we cannot use them for performance analysis. Instead we use the depth maps to project one RGB view to another in the video sequences

Table 6. Comparison of our method with techniques mentioned in [3] on Middlebury dataset using RMSE. Lower is better.

Method	Plastic	Baby	Bowling	Average
SSI [23]	1.7573	2.9638	6.4936	3.74
Linear Inter	1.3432	1.3473	1.4503	1.38
Cubic Inter	1.2661	1.3384	1.4460	1.35
FMM [53]	0.9580	0.8349	1.2422	1.01
GIF [32]	0.7947	0.6008	0.9436	0.78
FBF [4]	0.8643	0.6238	0.5918	0.69
EBI [2]	0.6952	0.6755	0.4857	0.62
Depthcomp [3]	0.6618	0.3697	0.4292	0.49
DDP (Ours)	0.4951	0.3232	0.5743	0.46

to compute and RGB re-projection error, which we quantify with Peak Signal to noise ratio (PSNR). It is defined as $PSNR = 20 \log_{10}(MAX_I / \sqrt{MSE})$, where MAX_I is the maximum value of the image and MSE is the mean squared error of the image. As we can see in Figure 8, DDP fills up holes and improves the PSNR. We also use the cross-bilateral hole filled depth maps included in the NYU v2 dataset as a baseline. We observe consistent qualitative and quantitative improvements using DDP compared to the cross-bilateral method.

4.5. Middlebury

Finally we compare to the baseline techniques described in Depthcomp [3] for Middlebury Dataset scenes [25, 41] in Table 6. We took the input images and disparity maps from Depthcomp [3] with the holes they created artificially in the disparity maps and compared to the baseline techniques they mention. The metric is Root Mean Square Error (RMSE) which is $\|D_{out} - D_{GT}\|_2$ where D_{out} is the output disparity and D_{GT} is the ground-truth disparity. Our average result is better than all of the other techniques in Table 6 for depth completion.

5. Conclusions

We have presented an approach to reconstruct depth maps from incomplete ones. We leverage the recently proposed idea of utilizing a neural network as a prior for natural color images, and introduced three new loss terms for depth map completion. Extensive qualitative and quantitative experiments on sequences from the Tanks and Temples, KITTI, NYU v2, Middlebury, and our own dataset demonstrated that the depth maps generated by our method were more accurate. An important future extension is improving the speed of the method, where an efficient version of the presented approach could be used for a real-time depth enhancement and 3D reconstruction pipeline. Further, the presented method could benefit from deeper understanding of the convergence properties of training deep image priors.



Figure 9. (a) Input RGB image and reconstructed pointcloud from (b) SGM (c) DDP (Ours) and (d) MVSNet depth images for Desk, Sundial, Stones, Office and Statue. Our reconstructions are more complete.

Supplementary

6. Reconstruction Pipeline

To illustrate the impact of the presented approach in the method section of the main paper, we show improvement in quality of reconstruction from a set of images. We leverage the improved depth images generated by our approach within standard multi-view reconstruction pipeline [15]. Some of the improved models generated by our method is shown in the Figure 9 as well as in the main paper.

High quality depth images are first generated using the presented deep depth prior method on SGM [24] depths. These depth images are then fused using Fusibile approach [15] to reconstruct the final 3d point cloud. Fusibile has certain hyperparameters that determine the precision and recall values for the resultant point cloud. These parameters include the disparity threshold and the number of consistent views. The disparity threshold determines the threshold of difference in disparity that is allowed for two points from two different depth maps to be merged. The number of consistent images shows the number of images in which a point has to have consistent depth values for it to appear in the merged point cloud. For different datasets we observed that different values for these hyperparameters gave the best results for SGM and our results. We report these hyperparameter values in Table 3 in the main paper as well.

7. Hyperparameters

In equation 2 in main paper for TnT [29] and our dataset: $\gamma_1 = 0.96$ $\gamma_2 = 0.02$; for all other dataset: $\gamma_1 = 0.98$ $\gamma_2 = 0.01$. In equation 3 in main paper: $\lambda_z = 0.8$. In equation 4 in main paper: $\lambda_I = 0.5$. In equation 5 in main paper: $\lambda_w = 0.5$. Hyper-parameters of the loss function are set through searching on a small subset (10 images randomly chosen) from each of Ignatius and Barn sequence in TnT and the validation set from KITTI [18, 36]. We use $N=2$ nearest neighbors while calculating warping based loss for multi-view datasets. For DDP we use a maximum and a minimum depth value to clip the depth maps for 7 different scenes in TnT dataset. We also add a constant value to all depths as mentioned in the main paper. These values are in Table 7. For TnT and our dataset, the initial learning rate is set to 0.00005, that is reduced by a factor of 0.01 after 12000 and 15000 epochs. The model is trained for 16000 epochs. For KITTI and NYU [47] datasets, the model is trained for 10000 epochs with initial learning rate of 0.00005.

8. SSIM Index

Structural Similarity index (SSIM) [58] is defined by the the equation 6,

$$SSIM(x, y) = \frac{(2\mu_x\mu_y + c_1)(2\sigma_{xy} + c_2)}{(\mu_x^2 + \mu_y^2 + c_1)(\sigma_x^2 + \sigma_y^2 + c_2)} \quad (6)$$

where, μ_x and μ_y are the averages of x and y , σ_x^2 and σ_y^2 are the variances of x and y , σ_{xy} is the covariance of x and y ,

Table 7. Minimum and maximum depth clipping values and the constant depth value added per scene before doing DDP for 7 scenes in TnT dataset

	min depth	max depth	constant
Ignatius	2.0	7.5	0.0
Barn	2.0	16.5	2.0
Caterpillar	2.0	7.5	0.0
Meetingroom	0.2	25.0	4.0
Truck	0.5	10.0	2.0
Courtroom	0.2	46.0	4.0
Church	0.2	16.0	4.0

$c_1 = (k_1 L)^2$ and $c_2 = (k_2 L)^2$ where L = dynamic range of pixel values and k_1 and k_2 are constants.

9. Qualitative Results

Along with the reconstructed models in the main paper we add 5 more results here in Figure 9. These 5 scenes are Desk, Sundial, Stones, Office and Statue respectively which we collect ourselves using the same technique as described in Section 4.3 in the main paper. We compare SGM depth based reconstruction, DDP (ours) depth based reconstruction and MVSNet [62] depth based reconstruction. The central portion of the radio on the desk gets filled in our reconstruction as well as the red tool box. The hidden portion of the sundial and the base of stones have holes in the SGM based reconstruction that gets partially filled in ours. The reflective computer screens and the holes on reflective desk in the Office scene gets partially filled. Finally we can see more trees and smaller holes in the Statue scene. We observe some holes in our reconstructions, in spite of the depth maps being complete. This is because the Fusibile parameters described in Section 6 remove inconsistent depths from multiple views.

References

- [1] H. Aanæs, R. R. Jensen, G. Vogiatzis, E. Tola, and A. B. Dahl. Large-scale data for multiple-view stereopsis. *International Journal of Computer Vision*, pages 1–16, 2016.
- [2] P. Arias, G. Facciolo, V. Caselles, and G. Sapiro. A variational framework for exemplar-based image inpainting. *International journal of computer vision*, 93(3):319–347, 2011.
- [3] A. Atapour-Abarghouei and T. P. Breckon. Depthcomp: real-time depth image completion based on prior semantic scene segmentation. 2017.
- [4] A. Atapour-Abarghouei, G. P. de La Garanderie, and T. P. Breckon. Back to butterworth—a fourier basis for 3d surface relief hole filling within rgb-d imagery. In *2016 23rd International Conference on Pattern Recognition (ICPR)*, pages 2813–2818. IEEE, 2016.
- [5] C. Banz, H. Blume, and P. Pirsch. Real-time semi-global matching disparity estimation on the gpu. In *2011 IEEE International Conference on Computer Vision Workshops (ICCV Workshops)*, pages 514–521. IEEE, 2011.
- [6] J. T. Barron and B. Poole. The fast bilateral solver. In *European Conference on Computer Vision*, pages 617–632. Springer, 2016.
- [7] M. Bleyer, C. Rhemann, and C. Rother. Patchmatch stereo—stereo matching with slanted support windows. In *Bmvc*, volume 11, pages 1–11, 2011.
- [8] M. Bleyer, C. Rother, P. Kohli, D. Scharstein, and S. Sinha. Object stereo—joint stereo matching and object segmentation. In *CVPR 2011*, pages 3081–3088. IEEE, 2011.
- [9] J.-R. Chang and Y.-S. Chen. Pyramid stereo matching network. In *Proceedings of the IEEE Conference on Computer Vision and Pattern Recognition*, pages 5410–5418, 2018.
- [10] Z. Chen, X. Sun, L. Wang, Y. Yu, and C. Huang. A deep visual correspondence embedding model for stereo matching costs. In *Proceedings of the IEEE International Conference on Computer Vision*, pages 972–980, 2015.
- [11] Z. Cheng, M. Gadelha, S. Maji, and D. Sheldon. A bayesian perspective on the deep image prior. In *CVPR*, pages 5443–5451, 2019.
- [12] A. Dai, A. X. Chang, M. Savva, M. Halber, T. Funkhouser, and M. Nießner. Scannet: Richly-annotated 3d reconstructions of indoor scenes. In *Proceedings of the IEEE Conference on Computer Vision and Pattern Recognition*, pages 5828–5839, 2017.
- [13] Y. Furukawa, B. Curless, S. M. Seitz, and R. Szeliski. Towards internet-scale multi-view stereo. In *2010 IEEE computer society conference on computer vision and pattern recognition*, pages 1434–1441. IEEE, 2010.
- [14] S. Galliani, K. Lasinger, and K. Schindler. Massively parallel multiview stereopsis by surface normal diffusion. In *2015 IEEE International Conference on Computer Vision (ICCV)*, pages 873–881, Dec 2015.
- [15] S. Galliani, K. Lasinger, and K. Schindler. Massively parallel multiview stereopsis by surface normal diffusion. In *Proceedings of the IEEE International Conference on Computer Vision*, pages 873–881, 2015.
- [16] Y. Gandelman, A. Shocher, and M. Irani. “Double-DIP”: Unsupervised image decomposition via coupled deep-image-priors. In *CVPR*, 2019.
- [17] S. K. Gehrig, F. Eberli, and T. Meyer. A real-time low-power stereo vision engine using semi-global matching. In *International Conference on Computer Vision Systems*, pages 134–143. Springer, 2009.
- [18] A. Geiger, P. Lenz, C. Stiller, and R. Urtasun. Vision meets robotics: The kitti dataset. *The International Journal of Robotics Research*, 32(11):1231–1237, 2013.
- [19] A. Geiger, M. Roser, and R. Urtasun. Efficient large-scale stereo matching. In *Asian conference on computer vision*, pages 25–38. Springer, 2010.
- [20] M. Goesele, N. Snavely, B. Curless, H. Hoppe, and S. M. Seitz. Multi-view stereo for community photo collections. In *2007 IEEE 11th International Conference on Computer Vision*, pages 1–8. IEEE, 2007.
- [21] N. Haala and M. Rothermel. Dense multi-stereo matching for high quality digital elevation models. *Photogrammetrie-Fernerkundung-Geoinformation*, 2012(4):331–343, 2012.

- [22] P. Heise, S. Klose, B. Jensen, and A. Knoll. Pm-huber: Patchmatch with huber regularization for stereo matching. In *Proceedings of the IEEE International Conference on Computer Vision*, pages 2360–2367, 2013.
- [23] D. Herrera, J. Kannala, J. Heikkilä, et al. Depth map inpainting under a second-order smoothness prior. In *Scandinavian Conference on Image Analysis*, pages 555–566. Springer, 2013.
- [24] H. Hirschmuller. Stereo processing by semiglobal matching and mutual information. *IEEE Transactions on pattern analysis and machine intelligence*, 30(2):328–341, 2007.
- [25] H. Hirschmuller and D. Scharstein. Evaluation of cost functions for stereo matching. In *2007 IEEE Conference on Computer Vision and Pattern Recognition*, pages 1–8. IEEE, 2007.
- [26] P.-H. Huang, K. Matzen, J. Kopf, N. Ahuja, and J.-B. Huang. Deepmvs: Learning multi-view stereopsis. In *Proceedings of the IEEE Conference on Computer Vision and Pattern Recognition*, pages 2821–2830, 2018.
- [27] M. Ji, J. Gall, H. Zheng, Y. Liu, and L. Fang. Surfacenet: An end-to-end 3d neural network for multiview stereopsis. In *Proceedings of the IEEE Conference on Computer Vision and Pattern Recognition*, pages 2307–2315, 2017.
- [28] A. Kendall, H. Martirosyan, S. Dasgupta, P. Henry, R. Kennedy, A. Bachrach, and A. Bry. End-to-end learning of geometry and context for deep stereo regression. In *Proceedings of the IEEE International Conference on Computer Vision*, pages 66–75, 2017.
- [29] A. Knapitsch, J. Park, Q.-Y. Zhou, and V. Koltun. Tanks and temples: Benchmarking large-scale scene reconstruction. *ACM Transactions on Graphics (ToG)*, 36(4):78, 2017.
- [30] P. Knöbelreiter and T. Pock. Learned collaborative stereo refinement. In *German Conference on Pattern Recognition*, pages 3–17. Springer, 2019.
- [31] P. Knobelreiter, C. Reinbacher, A. Shekhovtsov, and T. Pock. End-to-end training of hybrid cnn-crf models for stereo. In *Proceedings of the IEEE Conference on Computer Vision and Pattern Recognition*, pages 2339–2348, 2017.
- [32] J. Liu, X. Gong, and J. Liu. Guided inpainting and filtering for kinect depth maps. In *Proceedings of the 21st International Conference on Pattern Recognition (ICPR2012)*, pages 2055–2058. IEEE, 2012.
- [33] J. Lu, H. Yang, D. Min, and M. N. Do. Patch match filter: Efficient edge-aware filtering meets randomized search for fast correspondence field estimation. In *Proceedings of the IEEE conference on computer vision and pattern recognition*, pages 1854–1861, 2013.
- [34] W. Luo, A. G. Schwing, and R. Urtasun. Efficient deep learning for stereo matching. In *Proceedings of the IEEE Conference on Computer Vision and Pattern Recognition*, pages 5695–5703, 2016.
- [35] N. Mayer, E. Ilg, P. Hausser, P. Fischer, D. Cremers, A. Dosovitskiy, and T. Brox. A large dataset to train convolutional networks for disparity, optical flow, and scene flow estimation. In *Proceedings of the IEEE Conference on Computer Vision and Pattern Recognition*, pages 4040–4048, 2016.
- [36] M. Menze and A. Geiger. Object scene flow for autonomous vehicles. In *Conference on Computer Vision and Pattern Recognition (CVPR)*, 2015.
- [37] J. Pang, W. Sun, J. S. Ren, C. Yang, and Q. Yan. Cascade residual learning: A two-stage convolutional neural network for stereo matching. In *Proceedings of the IEEE International Conference on Computer Vision*, pages 887–895, 2017.
- [38] Z. Ren, J. Yan, B. Ni, B. Liu, X. Yang, and H. Zha. Unsupervised deep learning for optical flow estimation. In *Thirty-First AAAI Conference on Artificial Intelligence*, 2017.
- [39] O. Ronneberger, P. Fischer, and T. Brox. U-net: Convolutional networks for biomedical image segmentation. In *International Conference on Medical image computing and computer-assisted intervention*, pages 234–241. Springer, 2015.
- [40] D. Scharstein, H. Hirschmüller, Y. Kitajima, G. Krathwohl, N. Nešić, X. Wang, and P. Westling. High-resolution stereo datasets with subpixel-accurate ground truth. In *German conference on pattern recognition*, pages 31–42. Springer, 2014.
- [41] D. Scharstein and C. Pal. Learning conditional random fields for stereo. In *2007 IEEE Conference on Computer Vision and Pattern Recognition*, pages 1–8. IEEE, 2007.
- [42] D. Scharstein and R. Szeliski. A taxonomy and evaluation of dense two-frame stereo correspondence algorithms. *Int. J. Comput. Vision*, 47(1–3):7–42, Apr. 2002.
- [43] D. Scharstein, T. Tanai, and S. N. Sinha. Semi-global stereo matching with surface orientation priors. *2017 International Conference on 3D Vision (3DV)*, pages 215–224, 2017.
- [44] J. L. Schönberger, E. Zheng, M. Pollefeys, and J.-M. Frahm. Pixelwise view selection for unstructured multi-view stereo. In *European Conference on Computer Vision (ECCV)*, 2016.
- [45] T. Schops, J. L. Schönberger, S. Galliani, T. Sattler, K. Schindler, M. Pollefeys, and A. Geiger. A multi-view stereo benchmark with high-resolution images and multi-camera videos. In *Proceedings of the IEEE Conference on Computer Vision and Pattern Recognition*, pages 3260–3269, 2017.
- [46] A. Seki and M. Pollefeys. Sgm-nets: Semi-global matching with neural networks. In *Proceedings of the IEEE Conference on Computer Vision and Pattern Recognition*, pages 231–240, 2017.
- [47] N. Silberman, D. Hoiem, P. Kohli, and R. Fergus. Indoor segmentation and support inference from RGBD images. In *Computer Vision - ECCV 2012 - 12th European Conference on Computer Vision, Florence, Italy, October 7-13, 2012, Proceedings, Part V*, volume 7576 of *Lecture Notes in Computer Science*, pages 746–760. Springer, 2012.
- [48] S. N. Sinha, D. Scharstein, and R. Szeliski. Efficient high-resolution stereo matching using local plane sweeps. In *Proceedings of the IEEE Conference on Computer Vision and Pattern Recognition*, pages 1582–1589, 2014.
- [49] S. Song, S. P. Lichtenberg, and J. Xiao. Sun rgb-d: A rgb-d scene understanding benchmark suite. In *Proceedings of the IEEE conference on computer vision and pattern recognition*, pages 567–576, 2015.

- [50] T. Tanai and T. Maehara. Neural inverse rendering for general reflectance photometric stereo. In *ICML*, 2018.
- [51] T. Tanai, Y. Matsushita, and T. Naemura. Graph cut based continuous stereo matching using locally shared labels. In *Proceedings of the IEEE Conference on Computer Vision and Pattern Recognition*, pages 1613–1620, 2014.
- [52] T. Tanai, Y. Matsushita, Y. Sato, and T. Naemura. Continuous 3d label stereo matching using local expansion moves. *IEEE transactions on pattern analysis and machine intelligence*, 40(11):2725–2739, 2017.
- [53] A. Telea. An image inpainting technique based on the fast marching method. *Journal of graphics tools*, 9(1):23–34, 2004.
- [54] A. Tonioni, M. Poggi, S. Mattoccia, and L. Di Stefano. Unsupervised adaptation for deep stereo. In *Proceedings of the IEEE International Conference on Computer Vision*, pages 1605–1613, 2017.
- [55] S. Ullman. The interpretation of structure from motion. *Proceedings of the Royal Society of London. Series B. Biological Sciences*, 203(1153):405–426, 1979.
- [56] D. Ulyanov, A. Vedaldi, and V. Lempitsky. Deep image prior. In *CVPR*, pages 9446–9454, 2018.
- [57] O. Voynov, A. Artemov, V. Egiiazarian, A. Notchenko, G. Bobrovskikh, E. Burnaev, and D. Zorin. Perceptual deep depth super-resolution. In *Proceedings of the IEEE International Conference on Computer Vision*, pages 5653–5663, 2019.
- [58] Z. Wang, A. Bovik, H. Sheikh, and E. Simoncelli. Image quality assessment: From error visibility to structural similarity. In *IEEE transactions on image processing*, page 600–612. IEEE, 2004.
- [59] F. Williams, T. Schneider, C. Silva, D. Zorin, J. Bruna, and D. Panozzo. Deep geometric prior for surface reconstruction. In *CVPR*, pages 10130–10139, 2019.
- [60] O. Woodford, P. Torr, I. Reid, and A. Fitzgibbon. Global stereo reconstruction under second-order smoothness priors. *IEEE transactions on pattern analysis and machine intelligence*, 31(12):2115–2128, 2009.
- [61] Y. Xue, J. Chen, W. Wan, Y. Huang, C. Yu, T. Li, and J. Bao. Mvscrf: Learning multi-view stereo with conditional random fields. In *Proceedings of the IEEE International Conference on Computer Vision*, pages 4312–4321, 2019.
- [62] Y. Yao, Z. Luo, S. Li, T. Fang, and L. Quan. Mvsnet: Depth inference for unstructured multi-view stereo. In *Proceedings of the European Conference on Computer Vision (ECCV)*, pages 767–783, 2018.
- [63] Z. Yin, T. Darrell, and F. Yu. Hierarchical discrete distribution decomposition for match density estimation. In *Proceedings of the IEEE Conference on Computer Vision and Pattern Recognition*, pages 6044–6053, 2019.
- [64] J. Žbontar and Y. LeCun. Stereo matching by training a convolutional neural network to compare image patches. *The journal of machine learning research*, 17(1):2287–2318, 2016.
- [65] Y. Zhang and T. Funkhouser. Deep depth completion of a single rgb-d image. In *Proceedings of the IEEE Conference on Computer Vision and Pattern Recognition*, pages 175–185, 2018.
- [66] C. Zhou, H. Zhang, X. Shen, and J. Jia. Unsupervised learning of stereo matching. In *2017 IEEE International Conference on Computer Vision (ICCV)*, pages 1576–1584, Oct 2017.